Adsorption and incorporation of transition metals at the magnetite $Fe_3O_4(001)$ surface

Roland Bliem,[1] Jiri Pavelec,[1] Oscar Gamba,[1] Eamon McDermott,[2] Zhiming Wang,[1,*] Stefan Gerhold,[1] Margareta Wagner,[1] Jacek Osiecki,[3] Karina Schulte,[3] Michael Schmid,[1] Peter Blaha,[2] Ulrike Diebold,[1] and Gareth S. Parkinson[1,†]

[1]*Institute of Applied Physics, Vienna University of Technology, Vienna, Austria*

[2]*Institute of Materials Chemistry, Vienna University of Technology, Vienna, Austria*

[3]*MAX IV Laboratory, Lund University, Lund, Sweden*

(Received 25 June 2015; revised manuscript received 17 July 2015; published 26 August 2015)

The adsorption of Ni, Co, Mn, Ti, and Zr at the $(\sqrt{2} \times \sqrt{2})$R45°-reconstructed $Fe_3O_4(001)$ surface was studied by scanning tunneling microscopy, x-ray and ultraviolet photoelectron spectroscopy, low-energy electron diffraction (LEED), and density functional theory (DFT). Following deposition at room temperature, metals are either adsorbed as isolated adatoms or fill the subsurface cation vacancy sites responsible for the $(\sqrt{2} \times \sqrt{2})$R45° reconstruction. Both configurations coexist, but the ratio of adatoms to incorporated atoms depends on the metal; Ni prefers the adatom configuration, Co and Mn form adatoms and incorporated atoms in similar numbers, and Ti and Zr are almost fully incorporated. With mild annealing, all adatoms transition to the incorporated cation configuration. At high coverage, the $(\sqrt{2} \times \sqrt{2})$R45° reconstruction is lifted because all subsurface cation vacancies become occupied with metal atoms, and a (1×1) LEED pattern is observed. DFT+U calculations for the extreme cases, Ni and Ti, confirm the energetic preference for incorporation, with calculated oxidation states in good agreement with photoemission experiments. Because the site preference is analogous to bulk ferrite (XFe_2O_4) compounds, similar behavior is likely to be typical for elements forming a solid solution with Fe_3O_4.

DOI: 10.1103/PhysRevB.92.075440 PACS number(s): 68.47.Gh, 68.35.Fx, 68.43.Fg, 68.37.Ef

I. INTRODUCTION

Iron oxide surfaces play a central role in environmental chemistry and corrosion processes and are important in technologies such as microelectronics, biomedicine, and heterogeneous catalysis [1,2]. Due to the common usage of iron oxides as a catalyst support, the adsorption of catalytically active late transition metals has been extensively studied [3–9]. As is normal in metal-on-metal-oxide systems, three-dimensional (3D) nanoparticles typically form because the surface energy of the metal oxide is lower than the metal [10–12]. Considerably less effort has been invested studying adsorption of 3*d* transition and alkaline metals, despite the fact that they are known to promote catalytic reactions such as water-gas shift and ethylbenzene dehydrogenation, in which iron oxides are the active phase [13–17]. The role of the promoter, or even its location within the iron-oxide surface, is rarely known. Given their propensity for oxidation, 3*d* transition metals have been reported to react with metal oxide surfaces, usually with concomitant reduction of the host cations at the interface [18–20]. If the metal is soluble in the bulk of the oxide, diffusion into the bulk [21] competes with cluster formation at high temperature.

Here we study the adsorption of Ni, Co, Mn, Ti, and Zr on the (001) surface of Fe_3O_4 using a variety of surface science techniques. Adsorption can occur as cationic adatoms twofold coordinated to oxygen, as observed previously [12,22,23] for Au, Ag, and Pd, but incorporation into the Fe_3O_4 surface lattice is favored. The occupation of octahedral lattice sites is consistent with the structure of well-known bulk $M_{1-x}Fe_{2+x}O_4$ spinel ferrite phases, suggesting similar interfacial ternary oxide formation can be expected for other metals forming solid solution with Fe_3O_4. The formation of spinel ferrite phases on the conducting $Fe_3O_4(001)$ substrate makes this class of exciting materials accessible to surface science studies [24].

II. METHODS

The experiments were performed on a synthetic Fe_3O_4 single crystal grown using the floating zone method [25] and a natural Fe_3O_4 single crystal. No differences between the samples have been observed. Scanning tunneling microscopy (STM), low-energy electron diffraction (LEED), and x-ray photoelectron spectroscopy (XPS) data were acquired in a two-vessel ultrahigh vacuum (UHV) setup consisting of a preparation chamber (base pressure $<10^{-10}$ mbar) and an analysis chamber (base pressure $<7 \times 10^{-11}$ mbar) equipped with an Omicron μ-STM operated in constant current mode. The analysis chamber includes a commercial LEED setup, a VG Microtech dual anode x-ray source and a SPECS EA 10 Plus analyzer. The samples were prepared by cycles of sputtering with Ar^+ ions ($E_{Ar} = 1$ keV, ion current density $j_{sample} \approx 6.5\,\mu A/cm^2$, 10 min) and annealing in O_2 at 870 K ($p_{O_2} = 10^{-6}$ mbar, 10 min). Temperatures were measured with a K-type thermocouple attached to the sample holder. Because the thermocouple is not attached directly to the sample, the temperature readout can be up to 50 K too low at high temperatures. Up to 300 °C, a systematic uncertainty of the given temperatures of approximately ±20 K is possible. Additional XPS data for Ni, Co, and Ti were acquired in a separate UHV chamber equipped with a He flow cryostat, direct current sample heating, a twin anode (Al/Ag) x-ray

*Present address: Swiss Light Source, Paul Scherrer Institute, CH-5232 Villigen PSI, Switzerland.

†parkinson@iap.tuwien.ac.at

source with a Focus 500 monochromator, a SPECS Phoibos 150 analyzer, and a LEED setup. The analyzer has been calibrated (±0.1 eV) using a Au reference. In this system the sample was prepared by cycles of sputtering with Ne^+ ions ($E_{Ne} = 1$ keV, $j_{sample} \approx 2.3\ \mu A/cm^2$, 10 min) and annealing in O_2 (using a directional doser) at 870 K (chamber pressure $p_{O_2} = 8 \times 10^{-8}$ mbar, 15 min). The valence band and the Fe $2p$ photoemission experiments were performed at the Synchrotron Beamline I311 at the Max IV Laboratory in Lund, Sweden. After each injection the Au Fermi edge was measured as an energy reference. In all setups, Ni, Co, Ti, and Mn were deposited using Omicron electron-beam evaporators. Zr was deposited using a home-built Zr sputter source, similar in design to the one described by Mayr *et al.* [26]. The deposition rates (≈1 ML/min, 1 ML = 1 adatom per unit cell = 1.42×10^{14} atoms/cm^2) were calibrated using water-cooled or temperature-stabilized quartz crystal microbalances (QCM). The coverages given in the description of the data are determined by the QCM calibration, which is in line with estimates from STM images where counting of adsorbed atoms is possible.

The density functional theory (DFT) calculations were performed using the full-potential augmented plane wave+local orbital (APW+lo) method as implemented in WIEN2K [27]. We use the generalized gradient approximation with a Hubbard U ($U_{eff} = 3.8$ eV) to treat the highly correlated Fe, Ni, and Ti $3d$ electrons. Adsorption on magnetite was modeled on a force-relaxed 17-layer slab with inversion symmetry and a vacuum layer of 25 bohr (13.2 Å), built from a $(\sqrt{2} \times \sqrt{2})$ supercell of bulk cubic magnetite. The total energies were calculated with lattice parameters of bulk magnetite optimized for $U_{eff} = 3.8$ eV. Atomic sphere sizes of 0.98, 0.79, 1.0, and 1.0 Å were used for Fe, O, Ni, and Ti, respectively. The energies of the different configurations are compared to the sum of the total energies of two free metal atoms in an otherwise empty cell (same size as the 17-layer magnetite slab with vacuum layer) and a pristine magnetite slab. A plane-wave cutoff of $Rk_{max} = 7.0$, corresponding to 296.6 eV, was used, and the Brillouin zones of the surface models were sampled with a $3 \times 3 \times 1$ k mesh. The surface models were relaxed until all forces were below 1 mRy/bohr (26 meV/Å). A Fermi broadening of 0.08 eV was employed. STM simulations were performed in constant current mode using the Tersoff-Hamann approximation [28].

III. RESULTS

A. Experimental results

Magnetite crystallizes in the inverse spinel structure, based on an fcc oxygen lattice with interstitial iron atoms in octahedral (Fe_{oct}) and tetrahedral (Fe_{tet}) coordination to oxygen. The (001) surface forms a $(\sqrt{2} \times \sqrt{2})$R45° reconstruction, in which two subsurface Fe_{oct} vacancies (V_{Fe}) in the third (S-2) layer are correlated with an interstitial Fe_{int} with tetrahedral coordination in the second (S-1) layer [Fig. 1(a)] [29]. The corners of the black triangle in Fig. 1(a) indicate the lattice sites involved in the rearrangement in the first two subsurface layers. Previous work has shown that the additional Fe_{tet} in the subsurface blocks the adsorption of Au, Ag, and Pd above, resulting in just one stable adsorption site per $(\sqrt{2} \times \sqrt{2})$R45° reconstructed cell; twofold coordinated to surface oxygen where there is no subsurface Fe_{tet} neighbor [12,12,22,23,29–31]. The periodic rearrangement of the subsurface layers causes pairs of surface Fe_{oct} atoms to relax to alternating sides, resulting in the undulations of the rows of Fe_{oct} in the surface layer clearly evident in the DFT+U derived structural model [Fig. 1(a)]. These rows of Fe_{oct} appear as protrusions in STM images [Fig. 1(b)]. The cyan arrow highlights a bright

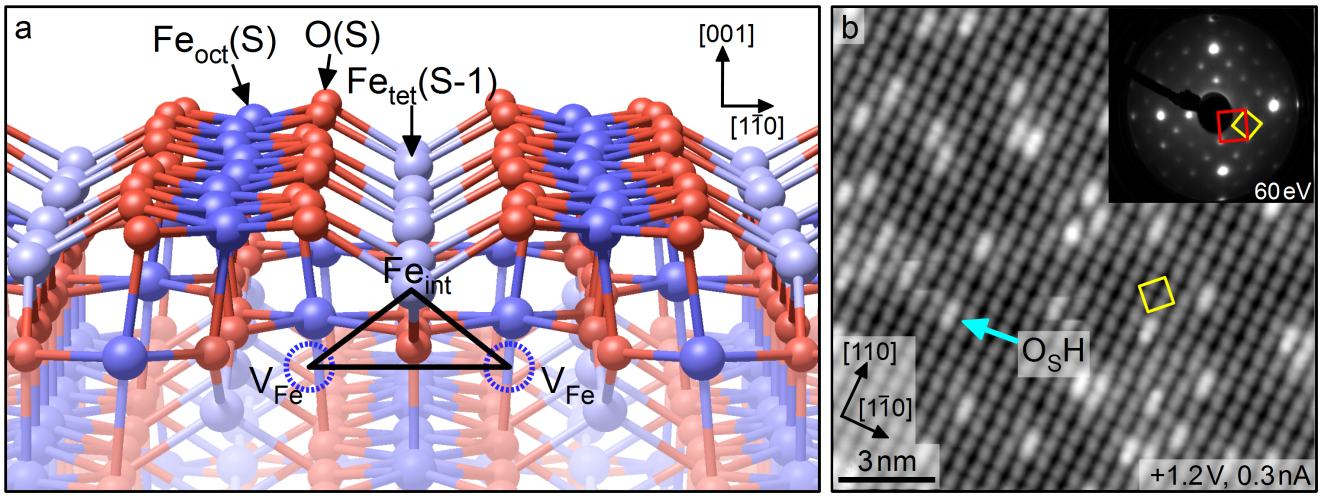

FIG. 1. (Color online) (a) DFT+U-optimized structural model of the $(\sqrt{2} \times \sqrt{2})$R45°-$Fe_3O_4$(001) surface. The outermost layer consists of a bulklike layer containing Fe in octahedral sites (Fe_{oct}, dark blue) and O (red). The first subsurface layer consists of tetrahedrally coordinated Fe (light blue): two bulklike Fe_{tet} and one additional Fe_{int} per $(\sqrt{2} \times \sqrt{2})$R45° unit cell. The black triangle indicates the region where the subsurface differs from the regular spinel structure. Two octahedral Fe atoms are missing from the subsurface Fe_{oct}-O layer (S-2) beneath Fe_{int} (dashed blue circles). (b) STM image of a clean Fe_3O_4(001) surface, in which the yellow square illustrates the $(\sqrt{2} \times \sqrt{2})$R45° unit cell. The bright double protrusions on the Fe rows (example highlighted by the cyan arrow) are due to surface hydroxyl groups, a common adsorbate at this surface. The inset shows a LEED pattern of the reconstructed Fe_3O_4(001) surface. The red and yellow squares highlight the (1×1) and $(\sqrt{2} \times \sqrt{2})$R45° periodicities, respectively.

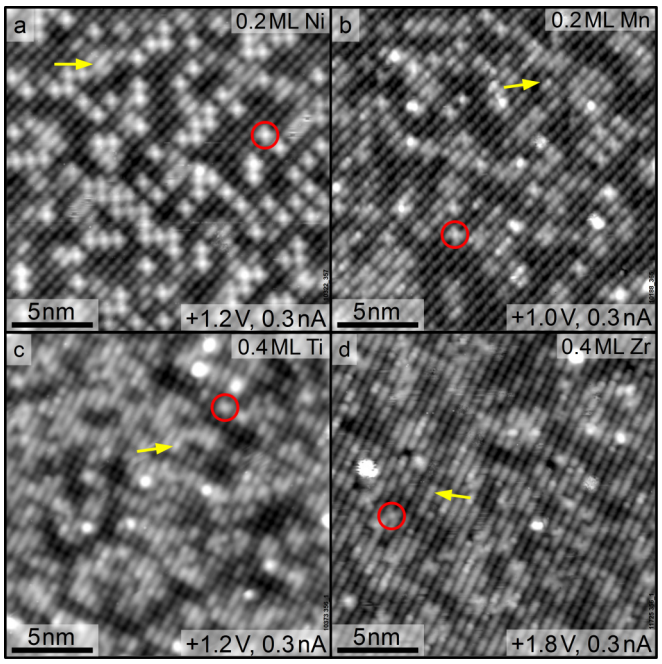

FIG. 2. (Color online) Overview of the adsorption of different metals at the $Fe_3O_4(001)$ surface at room temperature. STM images show that the deposited metals either adsorb as adatoms (red circles) or form bright surface features on the Fe_{oct} rows (yellow arrows). The ratio of these two configurations varies for the different metals. (a) 0.2 ML Ni: almost exclusively adatoms. (b) 0.2 ML Mn: few adatoms, many on-the-row features (c) 0.4 ML Ti: hardly any adatoms, high coverage of bright on-the-row features. (d) 0.4 ML Zr: very few adatoms, mainly on-the-row features.

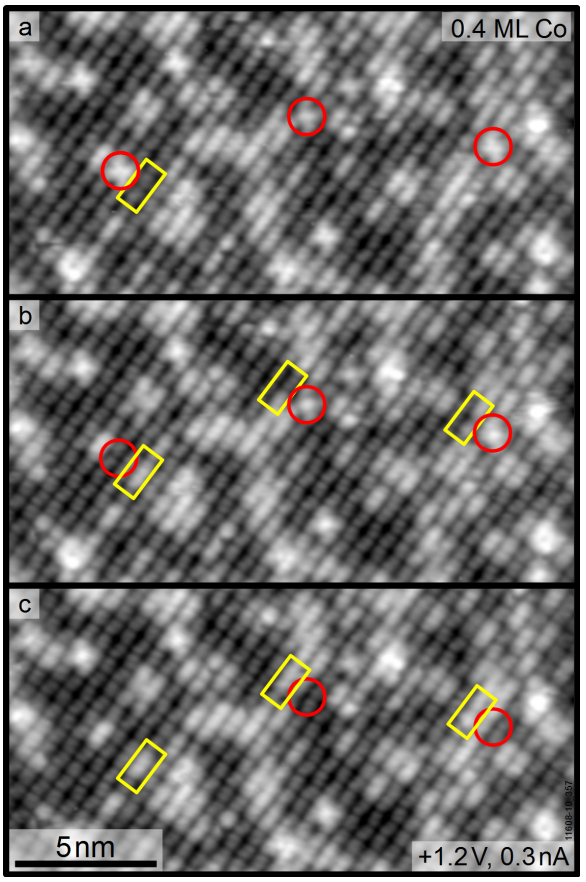

FIG. 3. (Color online) Co adatoms transition into on-the-row features at room temperature. STM image sequence (same area) of 0.4 ML $Co/Fe_3O_4(001)$ taken at room temperature. Three Co adatoms (red circles) are transformed into on-the-row features (encompassed by the yellow rectangles).

feature corresponding to a hydrogen atom bonding to surface oxygen (surface hydroxyl group) [31], a common adsorbate on this surface following UHV preparation. OH groups exhibit a characteristic hopping between two surface oxygen atoms and are thus easily distinguished from other surface species in STM movies [31,32]. The inset in Fig. 1(b) shows a LEED pattern of the $(\sqrt{2} \times \sqrt{2})R45^\circ$ reconstructed surface acquired at an electron energy of 60 eV.

In Fig. 2, STM images of low coverages of [Fig. 2(a)] Ni, [Fig. 2(b)] Mn, [Fig. 2(c)] Ti, and [Fig. 2(d)] Zr, deposited at room temperature onto the $Fe_3O_4(001)$ surface reveal element-specific differences in the adsorption behavior. For Ni, the main features are bright protrusions between the Fe rows. An example is highlighted by the red circle in Fig. 2(a). The appearance is similar to that of Au, Ag, and Pd adatoms [12,22,23] adsorbed on the surface twofold coordinated to oxygen, and since the number of such features corresponds approximately to the nominal coverage determined using the QCM, we assign this species to Ni adatoms. For Mn, the number of adatom features is clearly less than the deposited amount of 0.2 ML, and many new protrusions appear that are located directly at the Fe rows (yellow arrows). The protrusions appear similar to OH groups at 1 V but have a different apparent height depending on bias voltage and do not exhibit the characteristic hopping of OH groups [32] in STM movies. Although the deposited coverages of Ti and Zr are higher than the ones for Ni and Mn, almost no adatom features are observed. Instead, the surface contains immobile bright features located at the position of the surface Fe_{oct} rows, as observed for Mn (examples of such features are indicated by yellow arrows). The very bright, oval-like features in Figs. 2(b)–2(d) appear, change, or disappear during the acquisition of images and are thus attributed to weakly adsorbed molecules from the residual gas.

Figure 3 shows an STM image sequence acquired for Co in which adatoms transition from the adatom to the on-the-row configuration at room temperature. The initial state after deposition resembles $Mn/Fe_3O_4(001)$ [Fig. 2(b)], i.e., a mixture of adatoms and on-the-row features. Three Co adatoms are marked by red circles in Fig. 3(a). Between the first and second images, one adatom disappears and a new on-the-row feature (highlighted by a yellow rectangle) is observed. Similar site changes are observed for two other adatoms from Figs. 3(b) to 3(c). Whereas this transition can be observed for Co at room temperature, Ni adatoms require mild annealing to overcome the barrier to be converted into on-the-row features. In a thermal stability study (Fig. 4), 0.2 ML $Ni/Fe_3O_4(001)$ deposited at room temperature [Fig. 4(a)] was annealed at 423 K [Fig. 4(b)] and at 448 K [Fig. 4(c)] for 10 min and imaged using STM after cooling to room temperature. Because annealing required taking the sample out of the STM,

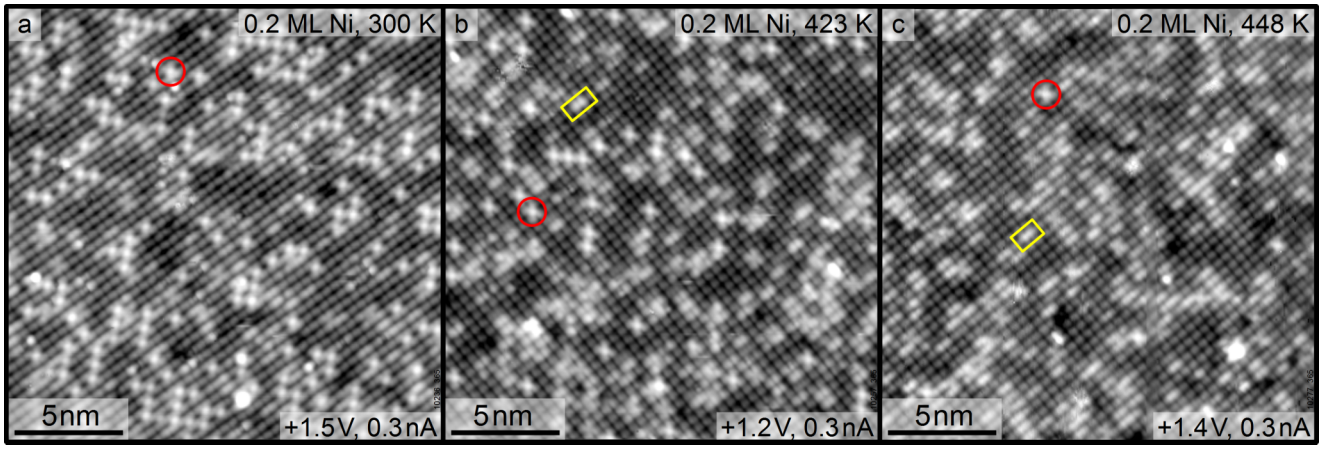

FIG. 4. (Color online) Thermal stability study of $Ni/Fe_3O_4(001)$ (different area in each image): Examples of adatoms and on-the-row features are highlighted by red circles and yellow rectangles. (a) At room temperature almost exclusively adatoms are observed. (b) After annealing to 423 K the number of adatoms is diminished. They coexist with an increased number of on-the-row features. (c) Almost all adatoms are converted to on-the-row features.

it was not possible to image the same area after heating. The as-deposited surface exhibits Ni adatoms only (examples highlighted by red circles), but after annealing adatoms and bright on-the-row features coexist [Fig. 4(b)]. After annealing to 448 K [Fig. 4(c)] the adatom phase is almost completely converted into the bright on-the-row features. Increasing the annealing temperature above 448 K causes the Ni to diffuse into the bulk and a clean Fe_3O_4 surface is recovered. STM images show neither adatoms nor on-the-row features. A $(\sqrt{2} \times \sqrt{2})$R45° LEED pattern is observed. In XPS measured after annealing to 870 K at a photon energy of 1050 eV the Ni $2p$ peak in XPS vanishes, indicating diffusion into the bulk of the crystal (not shown).

At metal coverages in excess of 1 ML, the $(\sqrt{2} \times \sqrt{2})$R45° reconstruction is lifted in favor of a (1×1) periodicity. Figure 5 shows STM images of the $Fe_3O_4(001)$ surface following deposition of 1 ML and 2.15 ML Ni at room temperature, together with the respective LEED patterns.

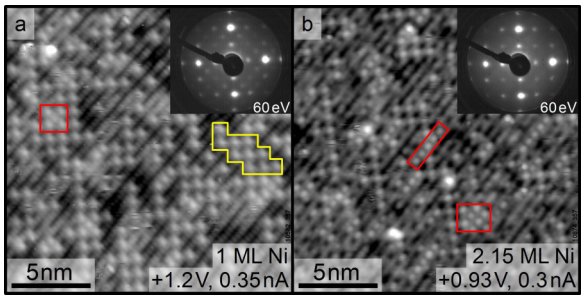

FIG. 5. (Color online) High coverage of $Ni/Fe_3O_4(001)$ deposited room temperature weakens the surface reconstruction and results in a higher fraction of on-the-row features: (a) 1 ML Ni: High adatom coverage, mostly adatoms with $(\sqrt{2} \times \sqrt{2})$R45° periodicity (yellow outline). A few $(\sqrt{2} \times \sqrt{2})$R45° unit cells are occupied by two Ni adatoms indicating an unreconstructed area (red square). The inset shows weak $(\sqrt{2} \times \sqrt{2})$R45° spots in the LEED pattern. (b) 2.15 ML Ni: Predominantly bright and straight Fe rows (surface filled by on-the-row features), larger patches of adatoms filling two sites per $(\sqrt{2} \times \sqrt{2})$R45° cell (red frames), unreconstructed LEED pattern.

In LEED, the diffraction spots associated with the $(\sqrt{2} \times \sqrt{2})$R45° reconstruction become weaker as the coverage is increased, and at 2.15 ML they are completely absent. In both cases, the density of Ni adatoms is significantly less than deposited; for the nominal 1 ML coverage it is 0.44 ML, suggesting the remainder forms on-the-row features. However, individual on-the-row features are difficult to discern at such a high coverage. Interestingly there are areas in which two Ni adatom protrusions are observed per unit cell (nearest neighbor distance of 6 Å, red outline) rather than one, as observed at low coverage (yellow outline). Given that the subsurface rearrangement is directly responsible for the $(\sqrt{2} \times \sqrt{2})$R45° periodicity, these data suggest that Ni modifies the subsurface restoring a bulklike spinel structure.

Photoelectron spectroscopy was used to determine the chemical state of the different metals. The XPS spectra in Fig. 6 show the $2p$ regions of Ni, Ti, and Co, as well as the Zr $3d$ peaks recorded at normal emission. In Fig. 6(a), Ni $2p$ spectra are shown for three different preparations: deposited at room temperature (red line), deposited at 200 K (blue line), and annealed to 465 K (black line). The room-temperature Ni $2p_{3/2}$ spectrum shows a peak at ≈855 eV with a low-binding-energy shoulder at ≈853.7 eV. This shoulder at ≈853.7 eV is significantly more pronounced when the Ni is deposited at low temperature. After annealing to 465 K, only the high-binding-energy component remains. Thus, two different species of Ni coexist in the surface region before annealing, in agreement with the results of the thermal stability study (Fig. 4). Both species have higher binding energy than metallic Ni, indicating that they bind to the lattice oxygen. The peak at 855 eV, dominant at RT and enhanced at high temperature, is associated with on-the-row features. The intensity shift to higher binding energy after annealing indicates that these on-the-row features contain Ni that is more oxidized than the Ni adatoms.

The Ti $2p$ spectrum in Fig. 6(b) shows symmetric peak shapes at binding energies indicating strongly oxidized Ti, similar to TiO_2 spectra [33]. The binding energies of the Co $2p_{3/2}$ peak, its satellite, and the satellite intensity are in good

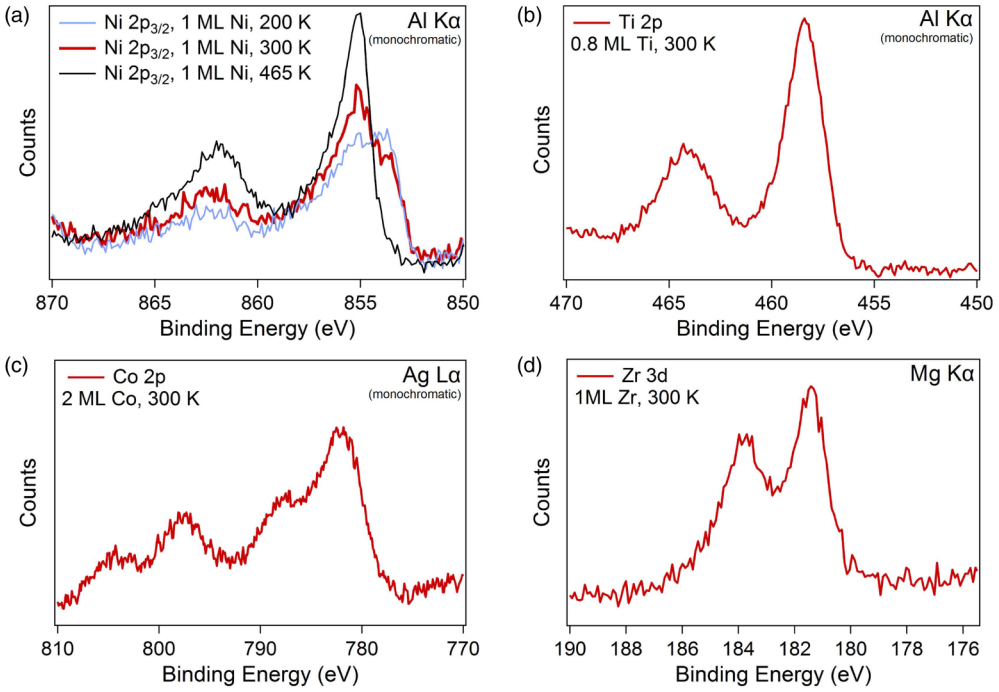

FIG. 6. (Color online) Normal-emission XPS spectra showing regions characteristic of the chemical state of the deposited metals. The red curves were acquired following deposition at room temperature. For Ni (a), additional spectra were acquired following deposition at low temperature (blue curve) and annealing to 465 K (black curve). Two different Ni species contribute to the 200 K and 300 K spectra. The peak positions in (b)–(d) indicate strongly oxidized metal species, in agreement with incorporation into the Fe_3O_4 lattice.

agreement with literature values [34] for CoO, indicating Co atoms with octahedral coordination to oxygen [Fig. 6(c)]. The Zr $3d_{5/2}$ peak at ≈181.4 eV [Fig. 6(d)] corresponds to Zr in mixed oxides [35], considerably shifted from the strongly oxidized state in ZrO_2.

Figure 7 shows the effect of metal deposition on the Fe_3O_4 substrate. The photoemission spectra were acquired at grazing angle (55° from the surface normal) and at low kinetic energies. The red curve in (a) shows that the Fe $2p_{3/2}$ spectrum of the pristine $(\sqrt{2} \times \sqrt{2})$R45°-$Fe_3O_4$(001) surface is dominated by Fe^{3+} (710.6 eV) [36]. Ni or Ti deposition (black and blue curves) causes the emergence of a clear Fe^{2+} shoulder (708.3 eV) [36]. Interestingly, although the coverage of Ni is significantly higher (1 ML) than that of Ti, the Fe^{2+} shoulder is more pronounced for the deposition of 0.4 ML Ti. This indicates that Ti deposition leads to a strong reduction of the surface Fe. Similar conclusions can be drawn from valence band photoemission. Figure 7(b) shows a significant intensity

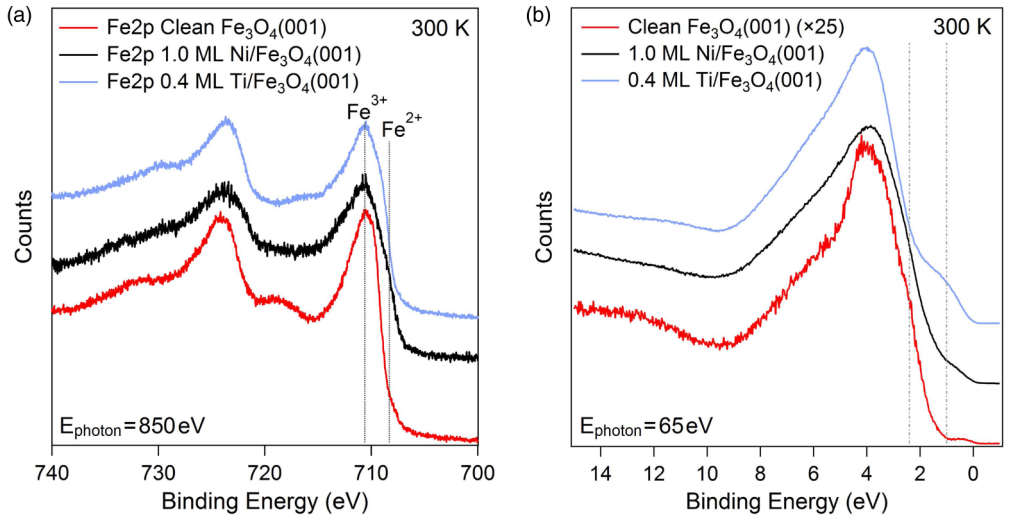

FIG. 7. (Color online) Comparison of photoemission spectra of clean Fe_3O_4(001), 1 ML Ni/Fe_3O_4(001), and 0.4 ML Ti/Fe_3O_4(001), both as deposited at room temperature. (a) In the Fe $2p_{3/2}$ region, an increase of Fe^{2+} after metal deposition is observed. (b) In the valence band spectrum, the metal deposition causes a significant increase of intensity at ≈1 eV.

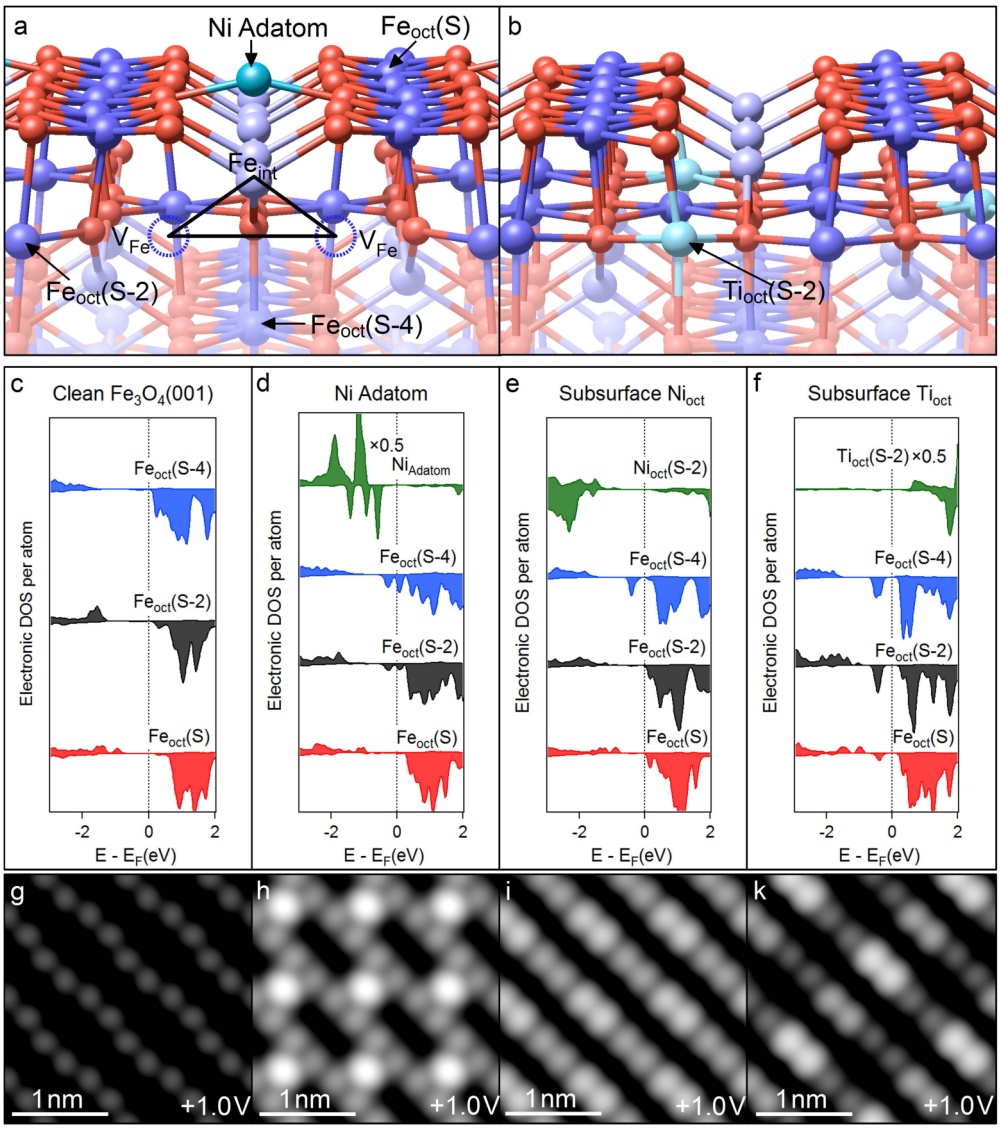

FIG. 8. (Color online) Summary of DFT calculations. (a) DFT+U optimized structural model of the reconstructed $Fe_3O_4(001)$ surface with a Ni adatom (side view). (b) Bulk-terminated structural model with a Ti atom substituting Fe in the energetically most favorable site (DFT+U optimized) for incorporated Ti and Ni atoms. [(c)–(f)] Density of states (DOS) of Ni/Ti and Fe_{oct} in the surface and first two subsurface layers for the clean surface and the favored configurations of Ni and Ti. [(g)–(k)] Simulated STM images of the four configurations based on a $(\sqrt{2} \times \sqrt{2})R45^\circ$ unit cell for the pristine surface (g), the Ni adatom (h), and the Ni_{oct}(S-2) configuration (i), and a (2×2) supercell for the Ti_{oct}(S-2) configuration (k).

shift from the shoulder at ≈2.2 eV, which originates from Fe^{3+}, to ≈1 eV, attributed [37] to Fe^{2+}.

B. DFT results

To ascertain the adsorption geometry of Ni and Ti atoms we performed DFT+U calculations. Figure 8(a) shows the optimized structural model for a Ni adatom, twofold coordinated to oxygen. For Ti, such a twofold coordination is not the ground state as the Ti adatom relaxes closer to the surface striving for higher coordination to oxygen, eventually finding a local force minimum involving distortions of the lattice at the surface. Since the experimental data show that metal adsorption induces a (1×1) periodicity, configurations in which the metal atoms replace one Fe atom within a bulklike termination were also considered. The surface octahedral site [Fe_{oct}(S)], a tetrahedral site in the first subsurface layer [Fe_{tet}(S-1)], and an octahedral site in the second subsurface layer [Fe_{oct}(S-2)] were selected as candidate sites. In these configurations the two Fe vacancies in the S-2 layer are filled by Fe_{int} and one Fe atom [for the Ni/Ti_{oct}(S) and Ni/Ti_{tet}(S-1) configurations] or one Ni/Ti atom [for the Ni/Ti_{oct}(S-2) configuration]. This occupation of the cation sites corresponds to a bulk-terminated $Fe_3O_4(001)$ surface with one Fe substituted by Ni/Ti. The structural model in Fig. 8(b) shows the force-relaxed $Fe_3O_4(001)$ slab with a Ti atom in an Fe_{oct}(S-2) site. This configuration is found to be energetically favorable for both Ni and Ti. Table I gives an overview of the energies of all configurations. The Ni_{oct}(S-2) geometry ($\Delta E = -3.39$ eV) is clearly preferred compared to the

TABLE I. Calculated energy differences for all studied configurations of Ni and Ti with respect to reconstructed $Fe_3O_4(001)$ and free atoms, site preference of the metals in a bulk spinel ferrite compound, calculated oxidation states, and experimental XPS peak energies. The comparison of DFT+U energies shows that Ti_{oct}(S-2) and Ni_{oct}(S-2) are the preferred configurations.

	Ni	Ti
Adatom energy	−3.21 eV	
M_{oct}(S) energy	−3.10 eV	−8.22 eV
M_{tet}(S-1) energy	−2.50 eV	−7.83 eV
M_{oct}(S-2) energy	−3.39 eV	−8.29 eV
Bulk ferrite site preference [38,39]	Ni_{oct}	Ti_{oct}
Oxidation state adatom (DFT+U)	+1	+4
Oxidation state M_{oct}(S-2) (DFT+U)	+2	+4
$2p_{3/2}$ binding energy (XPS)	855 eV/853.7 eV	458.4 eV

Ni adatom ($\Delta E = -3.21$ eV) and the Ni_{oct}(S) ($\Delta E = -3.10$ eV), which are approximately equivalent, and the Ni_{tet}(S-1) configuration ($\Delta E = -2.50$ eV). For Ti, the trend towards incorporation in the octahedral sites is even stronger; Ti_{oct}(S-2) is slightly preferred ($\Delta E = -8.29$ eV) over Ti_{oct}(S) ($\Delta E = -8.22$ eV). Incorporation in a tetrahedral geometry is unfavorable in comparison [Ti_{tet}(S-1): $\Delta E = -7.83$ eV]. Literature values [40] of the cohesive energy of TiO_2 indicate that the high energy differences for the Ti configurations result from the choice of free Ti atoms as an energy reference.

The valence state of the atoms can be determined by comparing the calculated total magnetic moments of a configuration to that of the pristine surface in order to estimate how much charge has been transferred to the surface. Additional information can be obtained from the magnetic moments and partial charges inside the atomic spheres. For the Ni adatom, the total magnetic moment of the slab changes by less than 0.1 μ_B, whereas the magnetic moment of Ni inside its atomic sphere is $|\boldsymbol{\mu}| = 1.0\ \mu_B$ and aligned with the Fe_{oct} spin orientation (spin up). The partial charges of the Ni adatom indicate a $4s^0 3d^9$-like state with one d electron in linear bond coordination to the surface oxygen atoms. Hence the Ni adatom donates one electron to the surface and assumes a +1 state. In the case of incorporated metal atoms, the major difference in the total magnetic moment of the slab with respect to the subsurface cation vacancy structure is caused by the rearrangement of Fe atoms in the S-1 and S-2 layers [$\Delta|\boldsymbol{\mu}| \approx 20\ \mu_B$ for the symmetric slab of Ni_{oct}(S), Ni_{oct}(S-2)]. If the contributions of the rearranged Fe and the magnetic moment of the Ni atom are subtracted from the total $\Delta|\boldsymbol{\mu}|$, the remaining difference gives a good estimate of the Ni charge donated to the slab. In the case of Ni_{oct}(S) and Ni_{oct}(S-2), the remaining magnetic moment is $\approx 2\mu_B$, corresponding to Ni^{2+}. The partial charges inside the atomic sphere are in good agreement with a Ni^{2+} state, showing a $4s^0 3d^8$-like configuration with unoccupied minority spin e_g-like orbitals for octahedrally coordinated Ni.

In all cases Ti is found to have small magnetic moments ($|\boldsymbol{\mu}| < 0.12\ \mu_B$ inside the atomic sphere) and negligible charge in the orbitals of $4s$ and $3d$ character. This allows the immediate conclusion that it assumes a Ti^{4+} state in all configurations. All these valence states agree well with the peak positions observed in the XPS spectra.

Figures 8(c)–8(f) show the electronic density of states (DOS) of the Ni/Ti atoms and of the surface layer and the first two subsurface layers of Fe_{oct} (normalized to the number of Fe atoms) for different configurations, i.e., the subsurface cation vacancy structure before metal deposition (c) and three energetically favorable configurations of Ni/Ti atoms [Ni adatom (d), Ni_{oct}(S-2) (e), and Ti_{oct}(S-2) (f)]. The position of the Ni electronic states for the Ni adatom indicates that the increased intensity at $\approx$1 eV below E_F in the photoemission experiments partially originates from Ni $3d$ occupied states close to the Fermi energy. For incorporated Ni and Ti, however, these states shift to higher binding energies or to unoccupied states. The comparison of the Fe_{oct} DOS shows that the increase in Fe^{2+} following metal deposition observed in photoemission is reflected in the DFT calculations by the emergence of an occupied spin-down electronic state close to the Fermi level in the first three Fe_{oct} layers. The Fe_{oct} occupied DOS in the surface layer remains largely unaltered. In the unoccupied states, however, a sharp increase of the unoccupied surface Fe_{oct} DOS close to the Fermi level is observed for the incorporation of Ni and Ti. In the first two subsurface layers, the Fe_{oct} atoms of the clean reconstructed $Fe_3O_4(001)$ surface exhibit hardly any occupied density of states close to the Fermi level. The adsorption of Ni adatoms causes a distinct peak at $\approx E_F - 0.3$ eV to appear in the Fe_{oct} DOS of both subsurface layers. The incorporation of Ni in the first subsurface octahedral layer (S-2) leads to a significant enhancement at $\approx E_F - 0.4$ eV in the second subsurface layer (S-4). Ti occupying an octahedrally coordinated subsurface Fe site leads to a considerable peak in the occupied subsurface Fe_{oct} DOS in the region between $E_F - 0.3$ and $E_F - 0.6$ eV.

All these results are consistent with an increase in Fe^{2+}observed in the valence band and Fe $2p$ photoemission spectra. The change from Fe^{3+} to Fe^{2+} is a direct result of the incorporation of additional metal atoms donating electrons to the slab. While in the case of Ni incorporation, the charge state of the Fe atoms in the (S-2) layer remains unaffected and Fe^{2+} is only found in deeper layers, the incorporation of Ti leads to one Fe^{2+} in the (S-2) layer and the emergence of a charge-ordered state from the (S-4) layer inwards, similar to that observed in the bulk-terminated $Fe_3O_4(001)$ structure [41,42].

In Figs. 8(g)–8(k) we show simulated STM images based on the minimum-energy DFT+U configurations described above. The clean $Fe_3O_4(001)$ surface [Fig. 8(g)] exhibits the undulating rows of surface Fe_{oct} atoms, as shown previously, and the addition of a Ni adatom results in a bright protrusion between the Fe rows [Fig. 8(h)], as expected simply on the basis of topography. The simulations of the incorporated Ni and Ti both exhibit a pair of particularly bright surface Fe_{oct} atoms, similar in appearance to the "on-the-row" features observed in experiment. Interestingly though, in the case of Ni, the bright surface Fe_{oct} atom pair is not located directly above the subsurface Ni but rather above the opposite row where the relocation of Fe_{int} into the octahedral site locally restores the bulk Fe_3O_4 structure. For Ti, a similar contrast enhancement occurs above the Fe_{oct}(S-2), but the STM contrast is dominated by a brighter Fe_{oct} pair located directly above the incorporated

Ti_{oct}(S-2) atom. A comparison of simulated STM images of the Ti_{oct}(S-2) and Ti_{oct}(S) configurations is shown in Fig. S1 (see the Supplemental Material) [43]. Note that for Ti_{oct}(S-2) the STM simulation is based on a 2×2 unit cell rather than the $(\sqrt{2} \times \sqrt{2})$R45° cell utilized previously. This choice ensures an area of the surface remains reconstructed, allowing easier comparison of the modified contrast to the clean Fe_3O_4(001) surface.

IV. DISCUSSION

Based on the experimental data and DFT calculations, a full picture of the adsorption behavior of metals at the Fe_3O_4(001) surface can be developed. Two distinct adsorption configurations exist following deposition at room temperature; adatoms and "on-the-row" features related to incorporation of metal atoms in the surface lattice. The adatom configuration is twofold coordinated to surface oxygen and similar to that reported previously for Au, Ag, and Pd [12,22,23]. Although the adatoms occupy a bulk-continuation tetrahedral site, it is important to note that they are in no way part of the spinel compound; while a bulk Fe atom should be 3+ and spin down in this site, the Ni adatom, for example, is close to 1+ and has a spin-up orientation.

For all metals studied here the incorporated configuration is clearly more stable. Upon deposition the barriers for incorporation are surpassed by the thermal energy of the evaporated atoms and the energy released by initial bond formation. The remaining adatoms are fully incorporated following mild annealing. Photoemission experiments show that the incorporated metal atoms are more oxidized and exhibit peak positions and line shapes that compare well with relevant bulk metal oxide compounds (e.g., the Co $2p$ core level shift and peak shape resemble that of Co^{2+} in CoO, and Ti $2p$ resembles that of Ti^{4+} in TiO_2). Our DFT calculations find that the lowest-energy configurations occur when the foreign metal atom occupies a subsurface octahedral site, and STM simulations of this structure compare very well with the "on-the-row" features observed in experiment. Note that the deposited metal fills one of the Fe_{oct} vacancies of the $(\sqrt{2} \times \sqrt{2})$R45° reconstruction, which induces Fe_{int} to occupy the other, thereby restoring the spinel structure in the surface. This is consistent with the (1×1) LEED pattern observed at high metal coverage as well as the emergence of a second stable adsorption site for adatoms.

The incorporation of the foreign metal atoms into the lattice modifies the electronic structure of the surface. Fe $2p$ XPS spectra clearly show an enhancement in Fe^{2+} in the surface region for all metals considered; the effect is strongest for Ti. The DFT+U calculations for incorporated Ni_{oct}(S-2) reveal that Fe_{oct} atoms in the surface Fe_{oct}-O layer remain Fe^{3+}, but that one Fe_{oct} in the subsurface (S-4) layer obtains a magnetic moment of $\approx 3.6\ \mu_B$, indicative of an Fe^{2+} oxidation state. For Ti this effect is stronger, resulting in Fe^{2+}-like magnetic moments ($\approx 3.5\mu_B$, $\approx 3.7\mu_B$) for two Fe_{oct} in the subsurface (S-2) layer. The enrichment in Fe^{2+}leads to an increase in the Fe_{oct} DOS near E_F [Fig. 7(b)], which DFT calculations find to be 100% spin polarized. These results suggest that doping the Fe_3O_4(001) surface with metals may be a viable route to tailor the spin polarization of the interface in Fe_3O_4 based spintronics devices.

While the general trend for incorporation is common to all five metals in the present study, the energy scale of this process is element specific. Ni forms mostly adatoms (Ni^{1+}) at room temperature, whereas Ti is almost exclusively incorporated into the surface (as Ti^{4+}). Co and Mn are somewhat intermediate, which raises the question whether there is an underlying trend. A simple approach to classify the affinity for oxidation of each metal is to consider the heat of formation of the most stable respective oxide, which decreases as one follows the sequence of elements from Ti to Ni across the periodic table [10]. This is in good agreement with the high DFT energy gain of incorporated Ti compared to Ni and reflected in experiment in the tendency to incorporate into the surface rather than forming adatoms with lower coordination to oxygen. An increased heat of oxide formation might also facilitate the incorporation into the lattice by providing the necessary energy to overcome the diffusion barrier for incorporation.

The incorporation of transition metal atoms within the Fe_3O_4 lattice invites comparison to the transition metal ferrites, ternary spinel compounds with the formula MFe_2O_4 or FeM_2O_4 (M = metal) [44]. The ferrites can be highly nonstoichiometric and are usually described in terms of a solid solution with Fe_3O_4. The M cation replaces Fe in either octahedral or tetrahedral sites depending on the metal, with the site preference depending on several factors, including relative cation size, oxidation state, and crystal field stabilization energy [44]. Our DFT+U prediction that Ni^{2+} and Ti^{4+} occupy octahedral sites is in good agreement with the site preference for the respective bulk ferrite phases [38,39]. As such, the incorporation of metals within the Fe_3O_4(001) surface can be viewed as the formation of a dilute ferrite phase localized at the surface or, alternatively, as an ultrathin ferrite film supported by a (conductive, lattice-matched) Fe_3O_4 substrate. This system can thus be used to study the surface properties of insulating ternary compounds such as $NiFe_2O_4$ (Fe_3O_4 will provide sufficient conductivity for STM and electron spectroscopies) and can serve as a template for the growth of thicker stoichiometric ferrite phases.

Considering the ferrite analogy, we suggest that the formation of ternary surface phases is likely not restricted to the small set of transition metals studied here but most likely extends to any metal that can form solid solutions with Fe_3O_4, much of the periodic table. Recently, there has been much interest in synthesizing novel spinel phases for energy applications [24,45] and incorporation at the Fe_3O_4(001) surface could be used to quickly investigate the potential stability and properties of new and exciting spinel phases predicted by theory. Our observation of Zr incorporation in the Fe_3O_4 lattice, for which there is no reported bulk ferrite analog, represents an early step in this direction.

V. CONCLUSION

The transition metals Ti, Mn, Co, Ni, and Zr were deposited onto the Fe_3O_4(001) surface. These transition metals are incorporated into the spinel lattice, filling subsurface Fe vacancies and locally lifting the $(\sqrt{2} \times \sqrt{2})$R45°

reconstruction. We suggest that such behavior is not exclusive to the metals studied but likely occurs for other metals that form solid solution with Fe_3O_4.

ACKNOWLEDGMENTS

G.S.P. and O.G. acknowledge support from the Austrian Science Fund Project No. P24925-N20. R.B. and E.M. acknowledge a stipend from the Vienna University of Technology and Austrian Science Fund doctoral college SOLIDS4FUN, Project No. W1243. U.D. and J.P. acknowledge support by the European Research Council advanced grant "OxideSurfaces." P.B. was supported by the Austrian Science Fund Project No. SFB-F41 ViCoM. The computational results were achieved (in part) using the Vienna Scientific Cluster (VSC). All authors acknowledge Z. Mao and T. J. Liu (Tulane University) for the synthetic sample used in parts of this work.

[1] R. M. Cornell and U. Schwertmann, *The Iron Oxides: Structure, Properties, Reactions, Occurrences and Uses* (Wiley-VCH, Weinheim, Germany, 2003).
[2] P. Tartaj, M. P. Morales, T. Gonzalez-Carreño, S. Veintemillas-Verdaguer, and C. J. Serna, Adv. Mater. **23**, 5243 (2011).
[3] W. Deng, C. Carpenter, N. Yi, and M. Flytzani-Stephanopoulos, Top. Catal. **44**, 199 (2007).
[4] H.-F. Wang, H. Ariga, R. Dowler, M. Sterrer, and H.-J. Freund, J. Catal. **286**, 1 (2012).
[5] B. Qiao, A. Wang, X. Yang, L. F. Allard, Z. Jiang, Y. Cui, J. Liu, J. Li, and T. Zhang, Nat. Chem. **3**, 634 (2011).
[6] Z. H. Qin, M. Lewandowski, Y. N. Sun, S. Shaikhutdinov, and H. J. Freund, J. Phys. Chem. C **112**, 10209 (2008).
[7] S. K. Shaikhutdinov, R. Meyer, M. Naschitzki, M. Bäumer, and H. J. Freund, Catal. Lett. **86**, 211 (2003).
[8] K. T. Rim, D. Eom, L. Liu, E. Stolyarova, J. M. Raitano, S.-W. Chan, M. Flytzani-Stephanopoulos, and G. W. Flynn, J. Phys. Chem. C **113**, 10198 (2009).
[9] J. C. Sharp, Y. X. Yao, and C. T. Campbell, J. Phys. Chem. C **117**, 24932 (2013).
[10] C. T. Campbell, Surf. Sci. Rep. **27**, 1 (1997).
[11] M. Bäumer and H.-J. Freund, Progr. Surf. Sci. **61**, 127 (1999).
[12] R. Bliem, R. Kosak, L. Perneczky, Z. Novotny, O. Gamba, D. Fobes, Z. Mao, M. Schmid, P. Blaha, U. Diebold, and G. S. Parkinson, ACS Nano **8**, 7531 (2014).
[13] M. Estrella, L. Barrio, G. Zhou, X. Wang, Q. Wang, W. Wen, J. C. Hanson, A. I. Frenkel, and J. A. Rodriguez, J. Phys. Chem. C **113**, 14411 (2009).
[14] W. Weiss and W. Ranke, Progr. Surf. Sci. **70**, 1 (2002).
[15] C. Rhodes and G. J. Hutchings, Phys. Chem. Chem. Phys. **5**, 2719 (2003).
[16] Y. Joseph, G. Ketteler, C. Kuhrs, W. Ranke, W. Weiss, and R. Schlogl, Phys. Chem. Chem. Phys. **3**, 4141 (2001).
[17] A. Miyakoshi, A. Ueno, and M. Ichikawa, Appl. Catal. A **216**, 137 (2001).
[18] A. K. See and R. A. Bartynski, Phys. Rev. B **50**, 12064 (1994).
[19] J.-M. Pan, U. Diebold, L. Zhang, and T. E. Madey, Surf. Sci. **295**, 411 (1993).
[20] U. Diebold, J. M. Pan, and T. E. Madey, Surf. Sci. **287-288, Part 2**, 896 (1993).
[21] J. Biener, J. Wang, and R. J. Madix, Surf. Sci. **442**, 47 (1999).
[22] Z. Novotny, G. Argentero, Z. Wang, M. Schmid, U. Diebold, and G. S. Parkinson, Phys. Rev. Lett. **108**, 216103 (2012).
[23] G. S. Parkinson, Z. Novotny, G. Argentero, M. Schmid, J. Pavelec, R. Kosak, P. Blaha, and U. Diebold, Nat. Mater. **12**, 724 (2013).
[24] R. Valenzuela, Phys. Res. Int. **2012**, 591839 (2012).
[25] Z. Q. Mao, Y. Maenoab, and H. Fukazawa, Mater. Res. Bull. **35**, 1813 (2000).
[26] L. Mayr, N. Köpfle, A. Auer, B. Klötzer, and S. Penner, Rev. Sci. Instrum. **84**, 094103 (2013).
[27] P. Blaha, K. Schwarz, G. K. H. Madsen, D. Kvasnicka, and J. Luitz, *WIEN2K, An Augmented Plane Wave + Local Orbitals Program for Calculating Crystal Properties* (Karlheinz Schwarz, Techn. Universität Wien, Austria, Wien, Austria, 2001).
[28] J. Tersoff and D. R. Hamann, Phys. Rev. Lett. **50**, 1998 (1983).
[29] R. Bliem, E. McDermott, P. Ferstl, M. Setvin, O. Gamba, J. Pavelec, M. A. Schneider, M. Schmid, U. Diebold, P. Blaha, L. Hammer, and G. S. Parkinson, Science **346**, 1215 (2014).
[30] Z. Novotny, N. Mulakaluri, Z. Edes, M. Schmid, R. Pentcheva, U. Diebold, and G. S. Parkinson, Phys. Rev. B **87**, 195410 (2013).
[31] G. S. Parkinson, Z. Novotný, P. Jacobson, M. Schmid, and U. Diebold, J. Am. Chem. Soc. **133**, 12650 (2011).
[32] G. S. Parkinson, N. Mulakaluri, Y. Losovyj, P. Jacobson, R. Pentcheva, and U. Diebold, Phys. Rev. B **82**, 125413 (2010).
[33] J. T. Mayer, U. Diebold, T. E. Madey, and E. Garfunkel, J. Electron Spectrosc. Relat. Phenom. **73**, 1 (1995).
[34] M. C. Biesinger, B. P. Payne, A. P. Grosvenor, L. W. M. Lau, A. R. Gerson, and R. S. C. Smart, Appl. Surf. Sci. **257**, 2717 (2011).
[35] A. Galtayries, R. Sporken, J. Riga, G. Blanchard, and R. Caudano, J. Electron Spectrosc. Relat. Phenom. **88-91**, 951 (1998).
[36] S. Kaya, H. Ogasawara, and A. Nilsson, Catal. Today **240, Part B**, 184 (2015).
[37] V. I. Anisimov, I. S. Elfimov, N. Hamada, and K. Terakura, Phys. Rev. B **54**, 4387 (1996).
[38] G. A. Sawatzky, F. Van Der Woude, and A. H. Morrish, Phys. Rev. **187**, 747 (1969).
[39] B. A. Wechsler, D. H. Lindsley, and C. T. Prewitt, Am. Mineral. **69**, 754 (1984).
[40] K. M. Glassford and J. R. Chelikowsky, Phys. Rev. B **46**, 1284 (1992).
[41] R. Pentcheva, F. Wendler, H. L. Meyerheim, W. Moritz, N. Jedrecy, and M. Scheffler, Phys. Rev. Lett. **94**, 126101 (2005).
[42] Z. Łodziana, Phys. Rev. Lett. **99**, 206402 (2007).
[43] See Supplemental Material at http://link.aps.org/supplemental/10.1103/PhysRevB.92.075440 for a simulated STM image of Ti in an octahedral site of the Fe_3O_4(001) surface compared to incorporation into the first subsurface layer.
[44] H. S. C. O'Neill and A. Navrotsky, Am. Mineral. **68**, 181 (1983).
[45] X. Zhang, V. Stevanović, M. d'Avezac, S. Lany, and A. Zunger, Phys. Rev. B **86**, 014109 (2012).